## Research Article Summary

# A radiation belt of energetic protons located between Saturn and its rings

*E. Roussos*†, P. Kollmann†, N. Krupp, A. Kotova, L. Regoli, C. Paranicas, D. G. Mitchell, S. M. Krimigis, D. Hamilton, P. Brandt, J. Carbary, S. Christon, K. Dialynas, I. Dandouras, M. E. Hill, W. H. Ip, G. H. Jones, S. Livi, B. H. Mauk, B. Palmaerts, E. C. Roelof, A. Rymer, N. Sergis, H. T. Smith*

*The list of author affiliations is available in the full article.*

**Corresponding author. Email: roussos@mps.mpg.de*

*†These authors contributed equally to this work.*

**INTRODUCTION:** Most magnetized planets are known to possess radiation belts, where high-energy charged particles are trapped in large numbers. The possibility that a radiation belt could exist also in the confined region between Saturn and its main rings has been proposed on the basis of remote sensing observations and simulations. It was not until the final 5 months of the Cassini mission that in situ measurements were obtained from this region with the Magnetosphere Imaging Instrument (MIMI). This paper provides an overview of these measurements and their interpretation.

**RATIONALE:** Saturn's main rings prevent the inward transport of trapped charged particles in the magnetosphere. Material from the outer radiation belts cannot directly access the low- altitude region within the rings. The isolation of this region allows the study of energetic particle source and loss processes because it is only in- directly coupled to the dynamics of the rest of the magnetosphere. Potential sources include cosmic ray albedo neutron decay (CRAND) and multiple-charge exchange, whereas losses are likely dominated by energy deposition and scattering of trapped particles by dust and atmospheric neutrals. All of these mechanisms involve charged particle interactions with mate- rials in space, meaning that MIMI measurements can provide information to probe the material itself—particularly the tenuous D-ring, the innermost component of Saturn's main rings, which is difficult to constrain by remote sensing observations.

**RESULTS:** We observed an inner radiation belt extending between 1.03 and 1.22 Saturn radii (1 $R_S$ = 60,268 km) at the equatorial plane, dominated by protons with energies from 25 MeV up to the giga–electron volt range. This belt is limited by the atmosphere at its inner edge and by the D73 ringlet (at 1.22 $R_S$), a component of the D-ring, at its outer boundary. Another ringlet (D68 at 1.12 $R_S$) splits the trapped particle population in two. The outer sector over- laps with the extended D-ring, and its intensity is reduced compared with that of the inner sector, owing to proton losses on ring dust. The proton angular distributions are highly anisotropic with fluxes that are orders of magnitude higher near the magnetic equator compared with fluxes of particles that can reach high latitudes. No time variability could be discerned in the >25-MeV proton population over the 5-month period of the observations. Trapping of lower-energy (tens of kilo–electron volt) protons was clearly observed in at least one case by imaging the emission of energetic neutral atoms (ENAs) coming from below ~1.06 $R_S$ (altitude < 3800 km). Energetic electrons (18 keV to several mega–electron volts) and heavy ions (27 keV per nucleon to hundreds of mega–electron volts per nucleon), if present, have fluxes close to or lower than the detection limit of the MIMI sensors.

**CONCLUSION:** The radial profile, the stability of the >25-MeV proton fluxes, and the lack of heavy ions are features consistent with a radiation belt originating from CRAND. The strong anisotropy of the proton distributions is primarily the result of proton losses in collisions with atmospheric neutrals, though an anisotropy in the production of CRAND protons from Saturn's rings may also con- tribute. The low-altitude, kilo–electron volt proton population is transient and derives from charge stripping of planetward ENAs, which are generated a

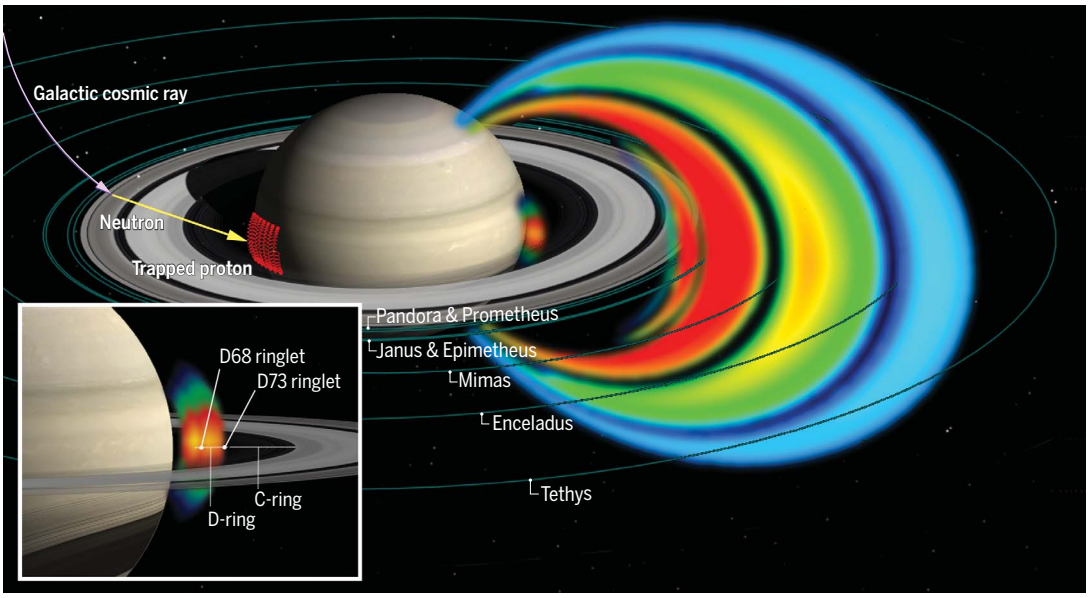


***Saturn's proton radiation belts.*** *Saturn's permanent proton radiation belt extends outward to the orbit of the moon Tethys but is segmented because of proton absorption by moons and rings. The innermost radiation belt (inset) threads through Saturn's D-ring and contains protons with energies up to several giga–electron volts, much higher than observed outside the main rings. These protons are among the b-decay products of neutrons, which are released through galactic cosmic ray collisions with Saturn's rings (CRAND process).*

## Research Article

# A radiation belt of energetic protons located between Saturn and its rings

E. Roussos[1]*†, P. Kollmann[2]†, N. Krupp[1], A. Kotova[3], L. Regoli[4], C. Paranicas[2], D. G. Mitchell[2], S. M. Krimigis[2,5], D. Hamilton[6], P. Brandt[2], J. Carbary[2], S. Christon[7], K. Dialynas[5], I. Dandouras[3], M. E. Hill[2], W. H. Ip[8], G. H. Jones[9,10], S. Livi[11], B. H. Mauk[2], B. Palmaerts[12], E. C. Roelof[2], A. Rymer[2], N. Sergis[5,13], H. T. Smith[2]

[1]*Max Planck Institute for Solar System Research, 37077 Goettingen, Germany.*
[2]*Johns Hopkins University Applied Physics Laboratory (JHUAPL), Laurel, MD 20723, USA.*
[3]*Institut de Recherche en Astrophysique et Planétologie, Université de Toulouse, Centre National de la Recherche Scientifique, Université Paul Sabatier, Centre National d'Etudes Spatiales, Toulouse, France.*
[4]*Department of Climate and Space Sciences and Engineering, University of Michigan, Ann Arbor, MI 48109, USA.*
[5]*Office of Space Research and Technology, Academy of Athens, Athens 11527, Greece.*
[6]*Department of Physics, University of Maryland, College Park, MD 20742, USA.*
[7]*Focused Analysis and Research, Columbia, MD 11043, USA.*
[8]*Institute of Astronomy, National Central University, 32001 Jhongli, Taiwan.*
[9]*Mullard Space Science Laboratory, University College London, Dorking, Surrey RH5 6NT, UK.*
[10]*The Centre for Planetary Sciences at University College London/ Birkbeck, London WC1E 6BT, UK.*
[11]*Southwest Research Institute, San Antonio, TX 78238, USA.*
[12]*Laboratory for Planetary and Atmospheric Physics, Space Sciences, Technologies and Astrophysics Institute, University of Liege, Liege, Belgium.*
[13]*National Observatory of Athens, 15236 Penteli, Greece.*

**Corresponding author. Email: roussos@mps.mpg.de*

*†These authors contributed equally to this work.*

*Saturn has a sufficiently strong dipole magnetic field to trap high-energy charged particles and form radiation belts, which have been observed outside its rings. Whether stable radiation belts exist near the planet and inward of the rings was previously unknown. The Cassini spacecraft's Magnetosphere Imaging Instrument obtained measurements of a radiation belt that lies just above Saturn's dense atmosphere and is decoupled from the rest of the magnetosphere by the planet's A- to C-rings. The belt extends across the D-ring and comprises protons produced through cosmic ray albedo neutron decay and multiple charge-exchange reactions. These protons are lost to atmospheric neutrals and D-ring dust. Strong proton depletions that map onto features on the D-ring indicate a highly structured and diverse dust environment near Saturn.*

During the proximal orbit phase of the Cassini mission (23 April to 15 September 2017), the spacecraft completed 22 crossings through the narrow gap between Saturn's upper atmosphere and its rings (Fig. 1). These orbits provided the opportunity to conduct in situ measurements of the local energetic charged particle environment with the Magnetosphere Imaging Instrument (MIMI) (1).

Observations of trapped particle radiation con- fined inward of Saturn's rings (inner trapping region) were obtained during Cassini's Saturn Orbit Insertion (SOI; 1 July 2004) through energetic neutral atom (ENA) imaging of this region using MIMI (2). Those observations revealed the emission of ENAs with energy of 20 to 50 keV per nucleon from a low-altitude, trapped ion population of the same energy, which was subject to charge-exchange with neutral atoms of Saturn's upper atmosphere. The ions

producing the low- altitude ENA emission are thought to derive from ENAs generated in the planet's middle magneto- sphere that propagate toward Saturn and impact its atmosphere (3, 4). Following their reionization through charge-stripping reactions in the planet's upper atmosphere, newly converted ions are temporarily trapped by the planet's magnetic field before charge exchange converts them back into the ENAs detected by MIMI (2). The altitude of the ion population driving this ENA emission is unknown but could extend to altitudes above Saturn's dense atmosphere (>1300 km), similar to the 0.06- to 1-MeV ions that were recently detected between 4300 and 18,000 km above Jupiter's 1-bar atmospheric level and were possibly generated by the same mechanism (multiple charge-exchange reactions) (5).

Higher-energy protons, at mega–electron volt energies and above, could be supplied to the inner trapping region through the cosmic ray albedo neutron decay (CRAND) process (6, 7). CRAND protons are among the b-decay products of secondary (albedo) neutrons formed in galac- tic cosmic ray (GCR) impacts on Saturn's atmosphere and/or its dense rings. Because neutrons are not bound by the planetary magnetic field, they can propagate from their generation site and through the trapping region, within which they may release their b-decay protons. The pro- cess is known to sustain the proton radiation belts of Earth and those of Saturn outside of its rings (main radiation belts) (8–12).

Although CRAND generates energetic protons near the planet, it has not been clear whether these particles can accumulate in large numbers and form a localized radiation belt. Quantitative models used to predict upper limits on the proton fluxes in this region (13) relied on a series of input parameter extrapolations and simplifying assumptions to determine the CRAND source rate and the loss rates of protons to atmospheric neutrals and to ring dust. It was not known if there would be a detectable signal from energetic protons across the D-ring (~1.11 to 1.24 $R_S$, where 1 $R_S$ = 60,268 km is Saturn's radius) (14) and its three ringlets—named D68, D72, and D73 and centered at 1.12, 1.19, and 1.22 $R_S$, respectively (15, 16)—all of which are contained within the inner trapping region. The D-ring properties were so poorly constrained that pre- dictions for the 10- to 60-MeV proton fluxes spanned more than two orders of magnitude (13), with the lowest values near MIMI's expected detection limits.

The simulations indicated that the dynamics of mega–electron volt protons in this inner radiation belt would be determined by different physical processes than those that affect the main radiation belts. Proton fluxes in Saturn's main radiation belts are limited by radial diffusion, which controls how fast these particles are distributed within the orbits of the planet's large icy moons, where they are subsequently absorbed (12, 17). Similarly, radial diffusion near the planet could act as a proton sink by gradually moving protons to the massive C-ring (1.24 to 1.53 $R_S$) and the dense atmosphere ð≲ 1:02 $R_S$ Þ. However, radial diffusion rates near the planet were projected to be extremely low (17, 18), so it was proposed that the intensity of the proton fluxes would be primarily determined by a balance of the CRAND source rate against losses of protons to dust and neutral gas. Losses to the equatorially confined dust can be transmitted along the magnetic field lines sampled by Cassini's high-inclination proximal orbit trajectory, allowing MIMI to obtain radial dust density scans of the D-ring system from a large distance (Fig. 1).

Understanding how the local dust and gas environment interacts with CRAND protons is simplified because proton populations in the inner trapping region are permanently isolated from the rest of the magnetosphere. Saturn's dense A- to C-rings form a ≈62,000-km-wide particle-absorbing corridor (1.24 to 2.27 $R_S$) that is impermeable to any magnetospheric particle transported inward of 2.27 $R_S$. Mixing of energetic particle populations near the planet from different source locations (10), which may occur at Earth and Jupiter and may complicate the interpretation of relevant measurements, is inhibited at Saturn. This filtering also applies to CRAND electrons, the other b-decay product of albedo neutrons, which were only recently detected around Earth (19). Furthermore, the strong magnetic field near Saturn forms a stable energetic charged particle trapping environment that is not perturbed by solar wind or magnetospheric transients that affect the magnetosphere at larger radii. The location of the inner trapping region establishes a constant source rate for CRAND protons and electrons because the primary GCR energies that drive CRAND and de- fine its source strength exceed 20 GeV (20). GCRs above this energy are not affected by the solar cycle (21). The stability of the CRAND source rate has previously proven useful in the under- standing of the magnetospheric processes that control the evolution of Saturn's main radiation belts (12).

**Instrumentation and methodology**

The MIMI instrument (1) comprises three dif- ferent sensors: the Low Energy Magnetospheric Measurement System (LEMMS), the Charge- Energy-Mass Spectrometer (CHEMS), and the Ion Neutral Camera (INCA).

LEMMS is a double-ended, charged particle telescope that can measure the energy and an- gular distribution of 27-keV to >300-MeV protons and of 18-keV to ~10-MeV electrons (22). Some LEMMS channels can also distinguish heavier mega–electron volt ions from protons but lack mass resolution (23). CHEMS can measure the energy, mass, and charge state of energetic ions between 3 and 220 keV per electron ($e^-$). INCA obtains ENA images of oxygen and hydrogen and high-sensitivity ion spectra in the energy range from 7 keV per nucleon to 8 MeV per nucleon.

The majority of our results are based on obser- vations by LEMMS channels P8 (>25 MeV $H^+$) and E7 (>300 MeV $H^+$ and >7 MeV $e^-$). These two channels achieve the most-efficient rejection of instrument-penetrating protons that can con- taminate the measurements. We occasionally use channel P9 (>60 MeV $H^+$ and >1 MeV $e^-$) because of its high-sensitivity, omnidirectional proton response. Unless otherwise stated, we quote channels P8, E7, and P9 by their proton energy response, because the respective measurements are dominated by protons.

Differential proton flux spectra were obtained using a forward model that reconstructs the >25- and >300-MeV count rates by convolving those channels' angular and energy response functions with predefined proton energy spectra and angu- lar distributions (22) (figs. S2 and S6). We also detected upper limits for lower proton energies or nonproton species when no signal was detected in LEMMS, CHEMS, and INCA (22) (fig. S7).

Magnetic mapping of the in situ measure- ments was performed by calculating the L-shell, equatorial pitch angle, and the loss cone through an empirical third-order magnetic field model (24). We define the L-shell value (L) as the dis- tance from the planet (in Saturn radii) that a field line crosses the magnetic equator. The equatorial pitch angle ($a_{eq}$) is the angle be- tween the proton velocity and the magnetic field at the magnetic equator, whereas the loss cone corresponds to the pitch angle below which the trapped particles reach under an al- titude of 1000 km and are absorbed in the dense atmosphere.

**Inner trapping region observations**

**Raw proton data**

The raw count rates of >25-, >300-, and >60-MeV protons are plotted in Fig. 2 as a function of L, from all instances when Cassini was magnetically connected to regions inward of Saturn's C-ring (table S1) (22). We can identify several features in this L-shell profile even before con- verting raw count rates to physical units.

We find a strong signal on magnetic field lines that map to the D-ring, even though trapped energetic protons at those L-shells cross through that ring every few seconds during their oscillation (bounce motion) along the magnetic field lines and thus are expected to experience heavy losses. The effects of proton absorption from two of the D-ring's ringlets are more severe. The count rate dropout that develops at the outer boundary of the trapping region maps to the location of the D73 ringlet (which has a width of 0.02 $R_S$), not the C-ring. This makes the radiation belt slightly narrower than predicted, because the presence of the ringlets was not taken into account in past simulations (13). A second drop in count rate, which splits the inner radiation belt into two main segments, is seen at the L-shell of the D68 ringlet. No obvious absorption signature is observed in association with the D72 ringlet.

In agreement with model predictions (13), the dense upper atmosphere limits the fluxes of trapped radiation toward the lowest L-shells. The omnidirectional >60-MeV proton measure- ments (Fig. 2C) registered counts at levels above the instrumental background down to L ~ 1.03, indicating that some minimal flux of mega– electron volt protons survives to at least 1800 km above the 1-bar atmospheric pressure level.

**Proton pitch angle distributions**

The large scatter of the mega–electron volt proton rates observed at any given L-shell (Fig. 2) can be attributed to changes in both the spacecraft's latitude and LEMMS's equatorial pitch angle pointing, $a_{eq}$ (fig. S1) (22). Reconstructing these two dominant dependencies (fig. S6) (22) requires the proton pitch angle distribution (PAD) to be much steeper than the one LEMMS resolves with its coarse angular resolution. If we de- scribe the PAD as o $\sin^N a_{eq}$ outside of the loss cone, we obtain that the power, N, ranges from 10 (at the D-ring) to 100 (near the atmosphere). For comparison, in Saturn's main proton radia- tion belts, this exponent is always less than ~6 (25–27). The small residuals between the observations and the reconstruction indicate that temporal variations, if present, must be less than the 1s statistical uncertainty in the LEMMS signal.

**Proton energy spectra (≥25 MeV)**

Differential proton fluxes were evaluated, assum- ing a spectral form that is a simple power law in energy and has a cutoff at 20 GeV. Even if Saturn's magnetic field can stably trap even higher en- ergies (28), those protons' circular motion around the magnetic field lines has a radius (gyroradius) that is comparable to the width of the trapping region (29). The resulting spectrum at L = 1.1, where the proton fluxes peak, is plotted in Fig. 3A.

We find that the proton spectrum is hard (i.e., flux decreases slowly with increasing en- ergy), with a spectral index of ~−1. For such a spectrum, relativistic protons ðgtrsim 0:9 GeVÞ could make a considerable contribution to the count rate of the >300-MeV channel. The fact that the >300-MeV proton channel recorded counts even when LEMMS was pointing well into the atmospheric loss cone (Fig. 2, A and B, and fig. S1A) is an indirect but independent verification that relativistic protons contribute to the measure- ments: Such counts may only come from >0.9-GeV instrument-penetrating protons (fig. S3) (22).

The shape of the proton spectrum may be more complex than the power law we assumed. For example, an additional spectral break might be expected at ~100 MeV, where the efficiency of CRAND neutron production changes (9, 30). Such a spectral shape cannot be unambiguously constrained with just the two proton channels used in this study. Still, even if we predefine its shape, the spectrum at >100 MeV remains hard, meaning that it is possible to constrain the proton fluxes at the giga–electron volt range. Our estimation of fluxes at 1 GeV is shown in the proton spectrum of Fig. 3A.

**L-shell distribution of protons**

The L-shell dependence of the differential proton fluxes at 300 MeV, deconvolved from their latitudinal and pitch angle dependencies (Fig. 4), shows that the innermost proton belt peaks around L = 1.1, just inward of the inner D-ring edge and in agreement with model predictions (13). That is a region where the combined material density from the D-ring dust and the atmospheric neutrals reaches a minimum, raising the proton fluxes.

The depth of the dropout attributed to the D68 ringlet has a pitch angle dependence (Fig. 4). With decreasing $a_{eq}$, the depth of the absorption becomes less pronounced, as expected for charged particles reaching high latitudes as they bounce along the magnetic field lines, well away from where proton losses to dust occur. No absorption signature is resolved at the location of the D72 ringlet, even after the raw counts are processed and deconvolved from their latitudinal and pitch angle dependencies.

**Low-altitude ENA emissions and upper limits of <25-MeV proton, ion, and electron fluxes**

Upper limits for <25-MeV protons, 18- to 832-keV electrons, and >5-MeV-per-nucleon helium and oxygen are also shown in Fig. 3, A and B. The results apply to L = 1.1 but are similar (within a factor of 3) to the entire L-shell range of the inner trapping region. The upper limits indicate a drop of the proton fluxes below ~25 MeV and negligible fluxes for light or heavy ions. Evidence for the absence of detectable electron fluxes at any energy to which LEMMS responds (18 keV to ~10 MeV ) is shown in

figs. S4 and S5 (22). The only resolvable trapped particle population with in situ data comes from >25-MeV protons.

Even though MIMI did not observe kilo– electron volt protons in situ, it detected remotely a 24- to 55-keV proton ENA emission from Saturn during its closest approach to the planet on 28 May 2017 (Fig. 5). The proton popu- lation responsible for this emission must have resided below the lowest altitude of ~3800 km sampled in situ by MIMI on that day. The non- detection of ENAs in several other cases that INCA had the correct pointing to observe (e.g., on 2 September 2017) suggests that the protons creating the ENA emission are transient.

## Interpretation of observations by MIMI

### Origin of mega–electron volt protons from ring CRAND

Several lines of evidence demonstrate that CRAND is the primary source process of the >25-MeV pro- ton belt: the presence of protons, the extension of the spectrum well above 300 MeV, the lack of any resolvable signal from heavy ions, the temporal stability, and the L-shell profile of the proton fluxes. The L-shell profile (Fig. 4) agrees qualitatively with that derived from simulations (13) for which a CRAND source was used as an input. Because this inner radiation belt is permanently decoupled from the rest of the magnetosphere, its detection alone constitutes direct evidence of the CRAND process.

At Saturn, CRAND may be catalyzed not only through the planet's atmosphere but also through the rings, from which we argue that the majority of CRAND protons originate. One reason is that the rings have a higher neutron yield than the planet's atmosphere (30). In addition, atmospheric neutrons that can reach the inner trapping region may only originate from a latitude be- low 36°, the region accessible to >40-GeV GCRs (20). Such GCRs have about one-fourth as much integral flux as the >20-GeV GCRs that reach the main rings, which also offer a 50% larger neutron production area than the limited atmo- spheric zone. The attribution of the inner radiation belt source to ring CRAND allows the separation of atmospheric and ring CRAND in the proton spectra of Saturn's main radiation belts (12, 17).

### Radiation belt and atmosphere coupling

The steep PAD inferred for both >25- and >300-MeV protons inward of the D-ring ðL ≲ 1:1Þ can be attributed to energy losses of these protons to Saturn's extended atmosphere. We demonstrate this in Fig. 4 by plotting the in- verse value of the average atmospheric density encountered by protons of different pitch angles as they move along the magnetic field (bounce- averaged atmospheric density) against the fluxes of 300-MeV protons. The inverse density profiles track the drop of the proton fluxes toward the planet, mostly for L ≲ 1:1. In a similar way, the terrestrial atmosphere is responsible for very steep proton PADs in Earth's radiation belts (31, 32).

### Radiation belt and D-ring coupling

For L ≳ 1:1, the inverse atmospheric density curves deviate from the deduced 300-MeV proton flux profiles, suggesting that the losses to the D-ring develop faster there. Using the previously derived scaling between D-ring density to proton flux (13), we estimate that the D-ring column density must be below $10^{-8}$ g/cm$^2$ (13), which is orders of magnitude lower than the corresponding A- and B-ring values [10 to 500 g/cm$^2$ (33–36)]. The partial, dust-driven depletion of the proton fluxes that we observe resembles the mega–electron volt proton interaction seen at Saturn's G-ring (L = 2.71) (17, 37, 38). Because losses to D-ring dust are stronger for equatorially mirroring particles ($a_{eq}$ ~ 90°), they are likely responsible for the reduced pitch angle anisotropy of protons estimated for L ≳ 1:1 (N ~ 10) compared with the anisotropy for L ≲ 1:1 (N ~ 100).

Even though the anisotropy for L ≳ 1:1 is rela- tively small compared with that for L < 1.1, it is still large compared with the anisotropy of protons in Saturn's magnetosphere ðN ≲ 6Þ. An additional source of proton anisotropy that could maintain such large N values may come from the CRAND process: Because CRAND protons are injected along the direction of their parent, b-decay neu- trons, their PAD may retain information about a preferential emission direction of neutrons from the rings. Simulations

show that an isotropic, ring neutron emission would lead to similarly isotropic proton PADs near the planet (18). The proton PAD at L $\gtrsim$ 1:1 may then hold evidence that the neutron injection from the rings is highly anisotropic. Such an anisotropy may constrain the dust size distribution in Saturn's A- to C-rings, as has been previously suggested (9, 30).

**Diversity of the D-ring ringlets**

Only two (D68 and D73) of the three ringlets of the D-ring are found to influence the L-shell profile of the proton fluxes. D73 has a normal optical depth of ~$10^{-3}$ (14), sufficient to deplete the energetic protons that LEMMS detects (39). D68 causes a strong reduction of proton fluxes (Figs. 2 and 4), whereas D72, which is as optically bright as D68, appears to have no impact on the trapped protons. The different influences of D68 and D72 on protons suggest that the former ringlet concentrates more mass in large grains and/or in its longitudinally confined arc, which has been observed remotely (14).

**Comparison with Earth's radiation belts**

Figure 3A shows the >25-MeV proton spectra from Saturn's inner trapping zone compared with those from L = 1.4 in Earth's magnetosphere, where the proton belt fluxes above 100 MeV peak (40). The comparison indicates that Earth fluxes are about an order of magnitude higher for energies below 400 MeV. This difference is mostly due to solar protons, which can reach low L-shells at Earth through radial transport, a source not available at Saturn due to the A- to C-rings. A turnover occurs beyond ~400 MeV and into the giga–electron volt range, where the projected proton fluxes at Saturn become stronger. Even though both Earth and Saturn produce CRAND protons in the giga–electron volt range, the 600-fold stronger magnetic mo- ment at Saturn allows a much more stable trap- ping of protons at relativistic energies (28). At Earth, trapped protons have been observed up to 2.2 GeV (32), whereas stable proton trapping is estimated to extend up to ~5 GeV (41).

**Comparison with Saturn's main radiation belts**

Proton fluxes in Saturn's main radiation belts drop more steeply with increasing energy (11, 23, 42) compared with our results for the innermost belt. Several explanations could account for this difference. Atmospheric CRAND from high latitudes, which can be generated by high-flux >0.5-GeV primary GCRs (20), has a stronger contribution to the main radiation belts than the contribution to the radiation belt near the planet. Magnetospheric radial diffusion becomes increasingly important at larger L-shells (12), whereas the proton trapping limit also drops to the range of ~1 GeV. We cannot exclude the possibility that part of the difference seen in the spectra is due to differing LEMMS calibration between the studies.

**Electron CRAND and additional energetic particle sources**

We did not detect any signature of electrons (presumably from CRAND) below 837 keV. This suggests that any electrons produced by CRAND are lost more efficiently than protons and can- not not build up detectable fluxes. The CRAND source rates at Earth and Saturn are comparable (6), so we can use this nondetection and make a rough order-of-magnitude estimation for the time scales of CRAND electron losses in the inner belt. If we assume that the input rate to 500-keV CRAND electron fluxes is $2.5 \times 10^{-2}$/(keV $cm^2$ sr s) in 1.5 hours, as measured at Earth (19), we find that CRAND electrons would exceed the upper detection limits shown in Fig. 3B within just 1 to 2 days. That is much shorter than the expected, year-long trapping time scales in the strong, axisymmetric magnetic field near Saturn. The nondetection indicates that 18- to 837-keV electrons are subject to losses, which act faster than a few days and could develop from electron scattering due to dust and neutrals, from wave-particle interactions, or even from weak radial flows, to which electrons are much more sensitive than the protons (43). Such flows may drive CRAND electrons onto the C-ring or the atmosphere within a few hours or days after their injection into the trapping region.

The upper limits for heavy mega–electron volt ions set tight constraints on the intensity of other, non-CRAND related source process that may operate in this region, such as the local pro- duction of energetic light ions through elastic collisions of CRAND protons with atmospheric neutrals (44).

## Low-altitude, kilo–electron volt proton radiation belt

The transient character of the low-altitude ENA emission confirms that its origin is in the vari- able ring current (2, 45). The 3800-km altitude limit inferred based on the lack of in situ kilo– electron volt proton detection when the ENA emission image was obtained (Fig. 5) can be fur- ther reduced to 2700 km if we rely on the value of the lowest L-shell for which LEMMS had the appropriate pointing to observe these protons in situ.

We find numerous differences when we com- pare our findings to similar observations at Jupiter. There, kilo–electron volt protons, which may have the same origin (charge-stripped ENAs), have fluxes that are three to five orders of mag- nitude above the upper limits estimated for Saturn (5) (Fig. 3A). It is possible that the high- ly structured internal magnetic field of Jupiter (46) enables ions produced through charge strip- ping in the denser layers of its upper atmosphere to drift around the planet along paths that ex- tend to higher altitudes, where the bounce- averaged density of neutrals to which they are exposed becomes negligible. That could allow ion fluxes to accumulate and become detectable before the ions complete a full orbit around the planet. The nonaxisymmetric terrestrial mag- netic field has a similar effect on CRAND elec- trons, as it allows them to accumulate only at a restricted longitude range where their orbit does not intersect the dense layers of our planet's at- mosphere (19). The axisymmetric magnetic field of Saturn, on the other hand, restricts ions pro- duced from charge stripping of ENAs to their high–atmospheric density generation altitude, severely limiting their lifetime and the extension of their population to the L-shells where MIMI made its in situ observations.

## Summary and conclusions

The proximal orbits of Cassini allowed the MIMI instrument to sample unexplored regions of Saturn's magnetosphere. Our measurements demonstrate that a radiation belt sector is present inward of Saturn's dense rings, despite the isolation of this region from the rest of the magnetosphere and its collocation with dust and atmospheric neutrals.

This radiation belt has two components. The primary one, bound by the planet's atmosphere and the D73 ringlet, originates from ring CRAND, comprises protons with energies extending from ~25 MeV into the giga–electron volt range, and appears to be stable throughout the 5-month observation period. Its structure is modified by the interaction of the CRAND protons with Saturn's atmosphere, the D-ring and its three ringlets. The secondary, low-altitude radiation belt component was observed only remotely through ENA imaging, is transient, and contains protons of kilo–electron volt energies. The nondetection of the kilo–electron volt proton population responsible for the ENA emission of the secondary belt, in the context of equivalent measurements from Jupiter and Earth, shows that Saturn's axisymmetric magnetic field suppresses the formation of stable, low-altitude radiation belts through multiple-charge exchange.

## REFERENCES AND NOTES

1. S. M. Krimigis et al., Magnetosphere Imaging Instrument (MIMI) on the Cassini Mission to Saturn/Titan. Space Sci. Rev. 114, 233–329 (2004). doi: 10.1007/s11214-004-1410-8

2. S. M. Krimigis et al., Dynamics of Saturn's magnetosphere from MIMI during Cassini's orbital insertion. Science 307, 1270–1273 (2005). doi: 10.1126/science.1105978; pmid: 15731445

3. J. F. Carbary, D. G. Mitchell, P. Brandt, E. C. Roelof, S. M. Krimigis, Statistical morphology of ENA emissions at Saturn. J. Geophys. Res. 113, A05210 (2008). doi: 10.1029/2007JA012873

4. K. Dialynas et al., The extended Saturnian neutral cloud as revealed by global ENA simulations using Cassini/MIMI measurements. J. Geophys. Res. 118, 3027–3041 (2013). doi: 10.1002/jgra.50295

5. P. Kollmann et al., A heavy ion and proton radiation belt inside of Jupiter's rings. Geophys. Res. Lett. 44, 5259–5268 (2017). doi: 10.1002/2017GL073730

6. J. A. Van Allen, B. A. Randall, M. F. Thomsen, Sources and sinks of energetic electrons and protons in Saturn's magnetosphere. J. Geophys. Res. 85, 5679–5694 (1980). doi: 10.1029/JA085iA11p05679

7. J. F. Cooper, "Innermost Van Allen Radiation Belt for High Energy Protons at Saturn" in AAS/Division for Planetary Sciences Meeting Abstracts #40 (Bulletin of the American Astronomical Society, 2008), vol. 40, p. 460.

8. S. F. Singer, Trapped Albedo Theory of the Radiation Belt. Phys. Rev. Lett. 1, 181–183 (1958). doi: 10.1103/ PhysRevLett.1.181

9. J. B. Blake, H. H. Hilton, S. H. Margolis, On the injection of cosmic ray secondaries into the inner Saturnian magnetosphere: 1. Protons from the CRAND Process. J. Geophys. Res. 88, 803–807 (1983). doi: 10.1029/JA088iA02p00803

10. R. S. Selesnick, M. K. Hudson, B. T. Kress, Direct observation of the CRAND proton radiation belt source. J. Geophys. Res. 118, 7532–7537 (2013). doi: 10.1002/2013JA019338

11. E. Roussos et al., Long- and short-term variability of Saturn's ionic radiation belts. J. Geophys. Res. 116, A02217 (2011). doi: 10.1029/2010JA015954

12. P. Kollmann, E. Roussos, A. Kotova, C. Paranicas, N. Krupp, The evolution of Saturn's radiation belts modulated by changes in radial diffusion. New Astron. 1, 872–877 (2017). doi: 10.1038/s41550-017-0287-x

13. P. Kollmann et al., MeV proton flux predictions near Saturn's D ring. J. Geophys. Res. 120, 8586–8602 (2015). doi: 10.1002/ 2015JA021621; pmid: 27812437

14. M. M. Hedman et al., Saturn's dynamic D ring. Icarus 188, 89–107 (2007). doi: 10.1016/j.icarus.2006.11.017

15. M. M. Hedman et al., Three tenuous rings/arcs for three tiny moons. Icarus 199, 378–386 (2009a). doi: 10.1016/ j.icarus.2008.11.001

16. M. Hedman, J. Burt, J. Burns, M. Showalter, Non-circular features in Saturn's D ring: D68. Icarus 233, 147–162 (2014). doi: 10.1016/j.icarus.2014.01.022

17. P. Kollmann, E. Roussos, C. Paranicas, N. Krupp,
D. K. Haggerty, Processes forming and sustaining Saturn's proton radiation belts. Icarus 222, 323–341 (2013).
doi: 10.1016/j.icarus.2012.10.033

18. J. F. Cooper, Nuclear cascades in Saturn's rings: Cosmic ray albedo neutron decay and origins of trapped protons in the inner magnetosphere. J. Geophys. Res. 88, 3945–3954 (1983). doi: 10.1029/JA088iA05p03945

19. X. Li et al., Measurement of electrons from albedo neutron decay and neutron density in near-Earth space. Nature 552, 382–385 (2017). doi: 10.1038/nature24642;
pmid: 29236693

20. A. Kotova, "Energetic particle tracking techniques and its application to the magnetosphere of Saturn," thesis, Universite Toulouse III – Paul Sabatier (2016).

21. I. G. Usoskin, K. Alanko-Huotari, G. A. Kovaltsov, K. Mursula, Heliospheric modulation of cosmic rays: Monthly reconstruction for 1951–2004. J. Geophys. Res. 110, A12108 (2005). doi: 10.1029/2005JA011250

22. Materials and methods are available as supplementary materials.

23. T. P. Armstrong et al., Energetic ions trapped in Saturn's inner magnetosphere. Planet. Space Sci. 57, 1723–1731 (2009).
doi: 10.1016/j.pss.2009.03.008

24. E. Roussos et al., Sources, sinks and transport of energetic electrons near Saturn's main rings. Geophys. Res. Lett. 10.1029/2018GL078097 (2018).

25. J. A. VAN Allen, M. F. Thomsen, B. A. Randall, R. L. Rairden, C. L. Grosskreutz, Saturn's Magnetosphere, Rings, and
Inner Satellites. Science 207, 415–421 (1980). doi: 10.1126/ science.207.4429.415; pmid: 17833551

26. S. M. Krimigis, T. P. Armstrong, Two-component proton spectra in the inner Saturnian magnetosphere. Geophys. Res. Lett. 9, 1143–1146 (1982). doi: 10.1029/GL009i010p01143

27. R. E. Vogt et al., Energetic Charged Particles in Saturn's Magnetosphere: Voyager 2 Results. Science 215, 577–582 (1982). doi: 10.1126/science.215.4532.577; pmid: 17771281

28. T. J. Birmingham, Charged particle motions in the distended magnetospheres of Jupiter and Saturn. J. Geophys. Res. 87, 7421–7430 (1982). doi: 10.1029/JA087iA09p07421

29. M. F. Thomsen, J. A. Van Allen, Motion of trapped electrons and protons in Saturn's inner magnetosphere. J. Geophys. Res. 85, 5831–5834 (1980). doi: 10.1029/JA085iA11p05831

30. J. F. Cooper, R. E. Johnson, P. Kollmann, E. Roussos, E. C. Sittler, "Plasma, neutral atmosphere, and energetic radiation environments of planetary rings," in Planetary Ring Systems: Properties, Structure, and Evolution, M. Tiscareno, C. Murray, Eds. (Cambridge Planetary Science Series, Cambridge Univ. Press, 2018), pp. 363–398.

31. R. S. Selesnick et al., Observations of the inner radiation belt: CRAND and trapped solar protons. J. Geophys. Res. 119, 6541–6552 (2014). doi: 10.1002/2014JA020188

32. O. Adriani et al., Trapped proton fluxes at low Earth orbits measured by the PAMELA experiment. Astrophys. J. 799, L4 (2015). doi: 10.1088/2041-8205/799/1/L4

33. S. J. Robbins, G. R. Stewart, M. C. Lewis, J. E. Colwell,
M. Sremčević, Estimating the masses of Saturn's A and B rings from high-optical depth N-body simulations and stellar occultations. Icarus 206, 431–445 (2010). doi: 10.1016/ j.icarus.2009.09.012

34. J. E. Colwell et al., "The structure of Saturn's rings" in Saturn from Cassini-Huygens, M. K. Dougherty, L. W. Esposito,
S. M. Krimigis, Eds. (Springer, 2009), pp. 375–412.

35. J. F. Cooper, J. H. Eraker, J. A. Simpson, The secondary radiation under Saturn's A-B-C rings produced by cosmic ray interactions. J. Geophys. Res. 90, 3415–3427 (1985).
doi: 10.1029/JA090iA04p03415

36. M. M. Hedman, P. D. Nicholson, The B-ring's surface mass density from hidden density waves: Less than meets
the eye? Icarus 279, 109–124 (2016). doi: 10.1016/ j.icarus.2016.01.007

37. J. A. Van Allen, Absorption of energetic protons by Saturn's ring G. J. Geophys. Res. 88, 6911–6918 (1983). doi: 10.1029/ JA088iA09p06911

38. M. M. Hedman et al., The source of Saturn's G ring. Science 317, 653–656 (2007). doi: 10.1126/science.1143964;
pmid: 17673659

39. C. Paranicas, A. F. Cheng, A Model of Satellite Microsignatures for Saturn. Icarus 125, 380–396 (1997). doi: 10.1006/ icar.1996.5635

40. R. S. Selesnick, D. N. Baker, S. G. Kanekal, V. C. Hoxie, X. Li, Modeling the Proton Radiation Belt With Van Allen Probes Relativistic Electron-Proton Telescope Data. J. Geophys. Res. 123, 685–697 (2018). doi: 10.1002/2017JA024661

41. R. S. Selesnick, M. D. Looper, R. A. Mewaldt, A theoretical model of the inner proton radiation belt. Space Weather 5, S04003 (2007). doi: 10.1029/2006SW000275

42. P. Kollmann et al., Energetic particle phase space densities at Saturn: Cassini observations and interpretations. J. Geophys. Res. 116, A05222 (2011). doi: 10.1029/2010JA016221

43. E. Roussos et al., Drift-resonant, relativistic electron acceleration at the outer planets: Insights from the response of Saturn's radiation belts to magnetospheric storms. Icarus 305, 160–173 (2018). doi: 10.1016/j.icarus.2018.01.016

44. R. S. Selesnick, R. A. Mewaldt, Atmospheric production of radiation belt light isotopes. J. Geophys. Res. 101, 19745–19757 (1996). doi: 10.1029/96JA01746

45. S. M. Krimigis, N. Sergis, D. G. Mitchell, D. C. Hamilton,
N. Krupp, A dynamic, rotating ring current around Saturn. Nature 450, 1050–1053 (2007). doi: 10.1038/nature06425; pmid: 18075586

46. J. E. P. Connerney et al., A New Model of Jupiter's Magnetic Field From Juno's First Nine Orbits. Geophys. Res. Lett. 45, 2590–2596 (2018). doi: 10.1002/2018GL077312

## ACKNOWLEDGMENTS

We thank M. Gkioulidou and J. Cooper for discussions, A. Lagg and J. Vandegriff for software support, and M. Kusterer for reducing the MIMI data. Funding: The German contribution of the MIMI/ LEMMS Instrument, E.R., and N.K. were in part financed by the German BMWi through the German Space Agency DLR under contracts 50 OH 0103, 50 OH 0801, 50 OH 0802, 50 OH 1101, and 50 OH 1502 and by the Max Planck Society. The JHUAPL authors, as well as D.H., K.D., and N.S., were partially supported by the NASA Office of Space Science under task order 003 of contract NAS5-97271 between NASA/GSFC and JHU and subcontracts between the University of Maryland and the Academy of Athens. G.H.J. is partially supported by the UK Science and Technology Facilities Council. French participation in the Cassini project

(A.K. and I.D.) is funded by CNES. L.R.'s contribution was supported by a NASA Living With a Star grant (NNX16AL12G). B.P. is supported by the PRODEX program managed by ESA in collaboration with the Belgian Federal Science Policy Office. Author contributions: All authors contributed to the discussion and interpretation of the data and the writing of the manuscript. E.R. and P.K. performed most data analysis tasks. E.R. updated the LEMMS sensor in-flight calibration and performed the response simulations. P.K. developed and applied the inversion method to obtain proton spectra and PADs. A.K. and L.R. evaluated the importance of CRAND anisotropy. G.H.J. produced graphics. Competing interests: The authors declare no competing interests. Data and materials availability: The Cassini/MIMI data are available through NASA's Planetary Data System at https://pds-ppi.igpp.ucla.edu/mission/Cassini-Huygens/CO/MIMI. We used the time periods listed in table S1. The results of the MIMI/LEMMS response simulations (22) are available in the Open Access Data Repository of the Max Planck Society (Edmond) at https://
edmond.mpdl.mpg.de/imeji/collection/SmWJCz268FQXdnvg.

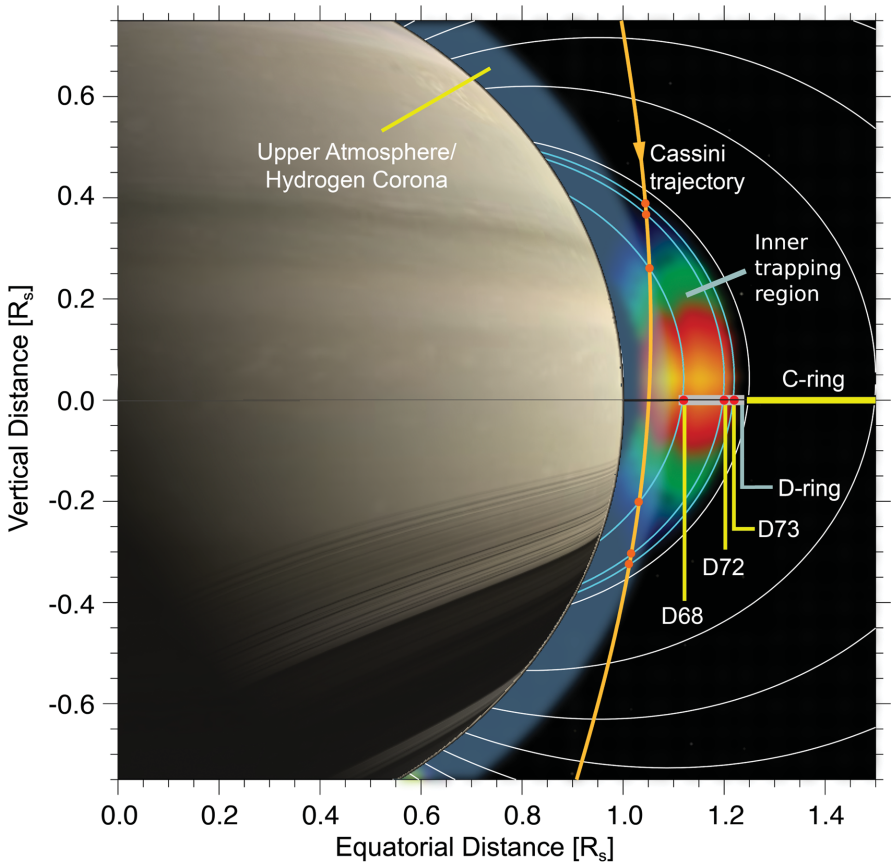


**Fig. 1. Geometry of the inner trapping region between Saturn's rings and atmosphere**. A schematic illustration of the inner trapping region is indicated by the color map. A typical Cassini proximal orbit trajectory is shown in orange. Cassini first intersects this region at ~20° north latitude and exits at a similar latitude to the south. Because trapped particles oscillate (bounce) along the magnetic field and through the equator every 2 to 3 s, Cassini can probe the effects of the D-ring's dust environment on these particles from high latitudes without directly crossing through it. The orange circles mark the locations along Cassini's trajectory where the effects of the D-ring's ringlets (D68, D72, and D73) on the trapped particle population can be transmitted along the magnetic field lines drawn in light blue. Other field lines (in white) are shown every 0.25 $R_S$ at the equatorial plane.

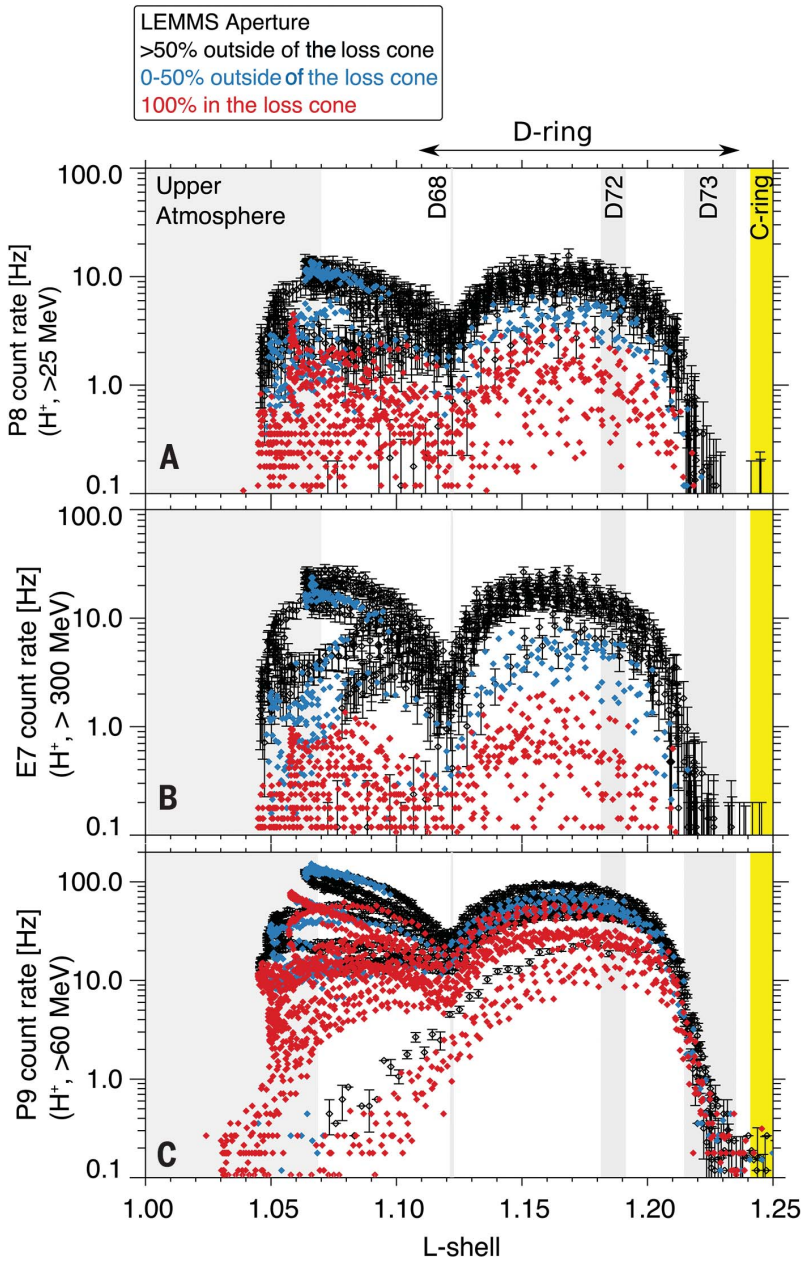


**Fig. 2. MIMI/LEMMS count rates as a function of magnetic L-shell.** Data are obtained from all proximal orbits (23 April to 15 September 2017) for regions that magnetically map inward of Saturn's C-ring (table S1) (22). All channels shown are dominated by protons and cover the energy range above 25 MeV. Count rates are averages of three consecutive samples (one data point per ~16 s). The points are color coded according to the percentage of LEMMS's aperture within the planetary loss cone (see legend). The channels in (A) and (B) roughly organize with pitch angle, whereas the channel in (C) does not, owing to its high sensitivity to sideways, instrument- penetrating protons.

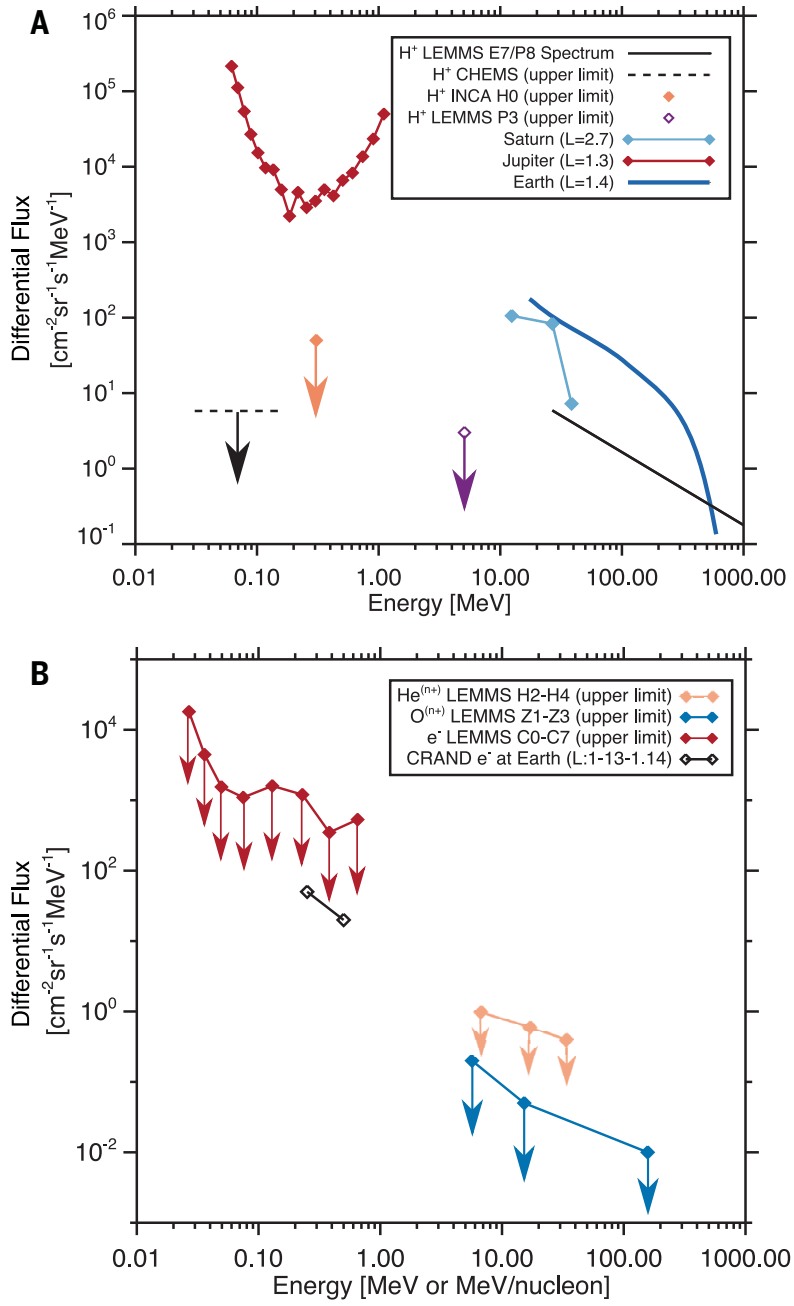


**Fig. 3. Energetic particle spectra and upper limits.** (A) Proton differ- ential flux spectrum of 25-MeV to >1-GeV protons (black line). As the PAD of the 25-MeV to ~1-GeV protons is highly anisotropic, a pitch-angle– averaged spectrum is plotted. All other symbols denote upper flux limits for lower-energy protons. For comparison, we also show a proton spectrum from L = 1.3 at Jupiter (5), from L = 2.7 at Saturn (11), and fromL=1.4($a_{eq}$~90°) at Earth (40). (B) Flux upper limits for ions and electrons. The H2-H4 and Z1-Z3 channels constrain the minimum atomic number (Z) of the ions detected(Z≥2andZ≥8, respectively), but, to define the channels' energies, we assume that these ions are helium and oxygen. On the horizontal axes, units are in mega– electron volts for protons and electrons and in mega– electron volts per nucleon for ions. The upper limits of electron fluxes can be compared with the maximum electron CRAND fluxes measured at Earth (19). All Saturn innermost belt measurements are from L = 1.1.

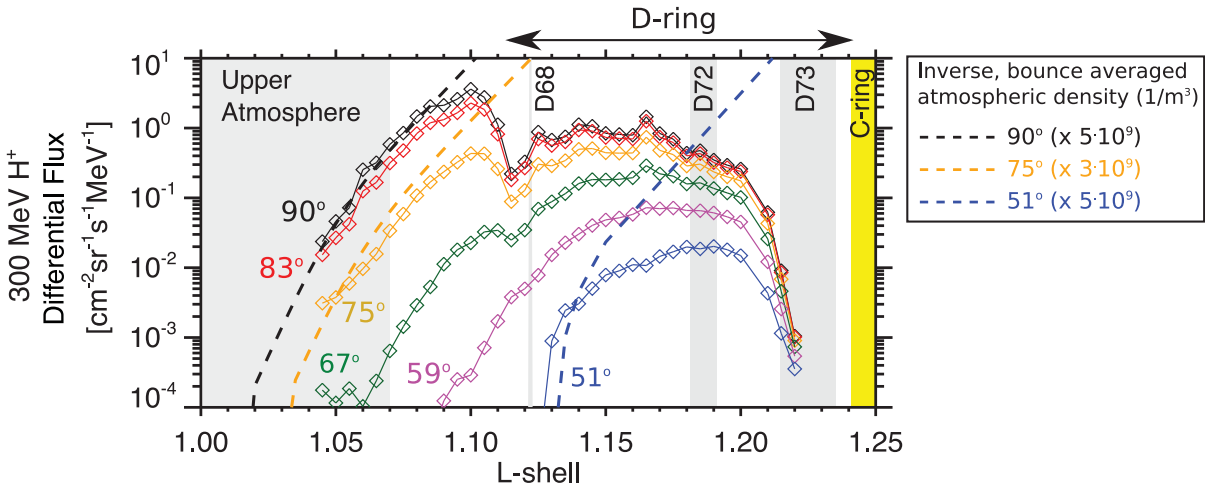


**Fig. 4. L-shell dependence of 300-MeV proton differential fluxes.** Different lines and colors correspond to different $a_{eq}$, as indicated in the figure. Fluxes are shown only where the inversion was successful. The progressively smaller extension of the radiation belts for decreasing pitch angles is due to the increasing size of the loss cone toward lower L-shells. The small offset of the central dropout from the L-shell of D68 is probably due to systematic errors associated with the magnetic field model. Overplotted are three curves showing the inverse of the bounce-averaged atmospheric density (13), scaled by appropriate factors (see legend) for a better comparison with the proton fluxes. The small difference in the adopted scaling factors accounts for the inconsistencies between the proton flux profiles and the atmospheric model used.

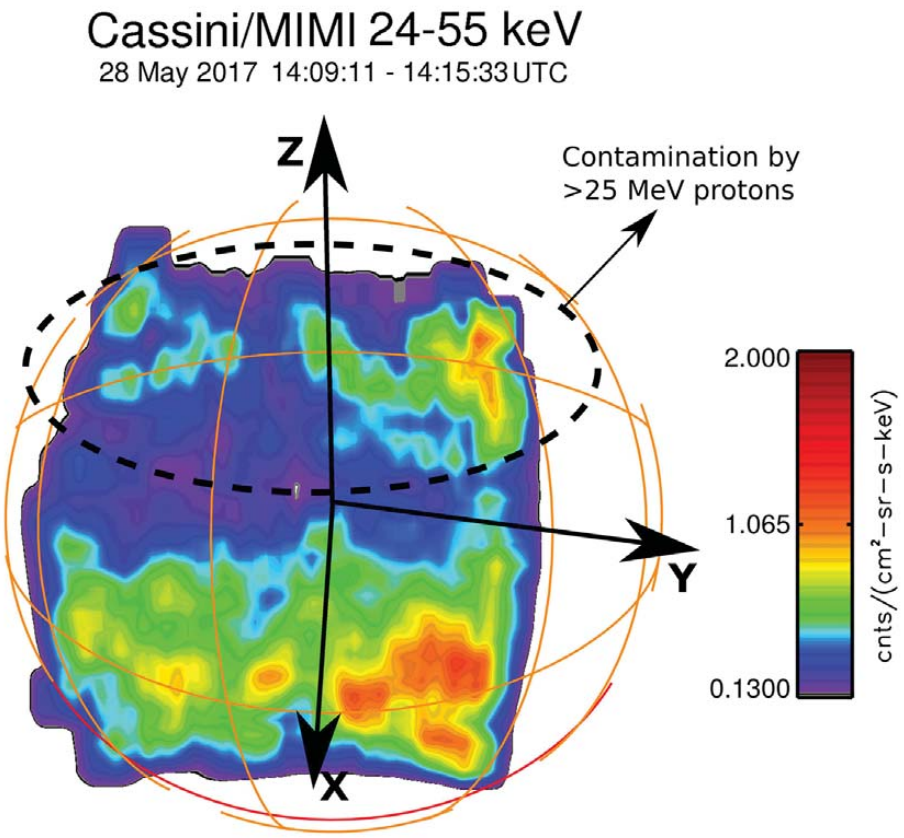


**Fig. 5. Imaging of the low-altitude ENA emission**. An image of Saturn in 24- to 55-keV proton ENAs obtained with the MIMI/INCA camera on 28 May 2017 is shown. Cassini was 1.13 $R_S$ away from Saturn's center and at a north latitude of 20.45°. The grid of Saturn is overlaid for reference, with the red grid line marking the equator. Latitude and longitude grid lines are shown every 10°. The emission from the low- altitude kilo–electron volt ion radiation belt, observed also at SOI in 2004 (2), is the one from lower latitudes. The emission that appears to come from higher latitudes is due to contamination of the INCA measurements by the >25-MeV protons observed by LEMMS. A smoothing has been applied to the image to enhance visibility of the low-altitude emission and to reduce signal fluctuations due to low counting statistics. The boundaries of the emission are due to INCA's field of view. The coordinate system displayed has its origin at the center of Saturn, with the z axis pointing north. The other two axes are along Saturn's equatorial plane, with the y axis pointing toward dusk and the x axis toward local noon.